

# Monitoring Geohazards near Pipeline Corridors with an Advanced InSAR Technique and Geomechanical Modelling



*Challenges from North to South  
Des défis du Nord au Sud*

Jayanti Sharma, Mike Kubanski, Jayson Eppler, Jennifer Busler  
*MDA Systems Ltd., Richmond, BC, Canada*  
Mirko Francioni, Doug Stead, John Clague  
*Simon Fraser University, Burnaby, BC, Canada*  
Marc-André Brideau  
*BGC Engineering Inc., Vancouver, BC, Canada*

## ABSTRACT

Surface displacements derived from Interferometric Synthetic Aperture Radar (InSAR) for the monitoring and risk assessment of geohazards near pipeline corridors are presented. The InSAR results are integrated with GIS analyses and field data to define geologic and preliminary geomechanical models using the InSAR-derived displacements and GIS-derived geological features as a constraint. Geohazard monitoring is demonstrated over the Fels Glacier in Alaska, which is bordered by active, deep-seated, slowly deforming slopes with the potential for generating large landslides that could damage the nearby Trans-Alaska Pipeline and Richardson Highway.

## RÉSUMÉ

Des mouvements de surfaces déduits des techniques de radar interférométrique à ouverture synthétique (InSAR), utilisées pour la surveillance et l'évaluation des risques associés aux aléas géologiques près de corridors d'un pipeline, sont présentés. Les résultats InSAR sont intégrés aux analyses SIG et aux données de terrain afin de définir des modèles géologiques et géo-mécaniques préliminaires utilisant les déplacements obtenus de l'InSAR et les particularités géologiques obtenues de l'analyse SIG comme contraintes de modélisation. La surveillance d'aléa géologique est démontrée pour le site du glacier de Fels en Alaska qui borde une profonde et lente déformation gravitationnelle active qui a le potentiel de générer de grands glissements pouvant endommager le Pipeline Trans-Alaska et l'Autoroute Richardson qui sont tous deux situés à proximité.

## 1 INTRODUCTION

Pipeline owners and operators face numerous operational challenges from geohazards in pipeline corridors including landslides, slope creep, subsidence, and permafrost degradation. Current monitoring solutions used by industry include borehole instrumentation, site inspections, and conventional surveys. Key challenges of these methods include obtaining high accuracy measurements over a broad geographic area including areas outside the pipeline right-of-way, and early and accurate identification of developing geotechnical hazards.

In this paper we present surface displacement results derived from Interferometric Synthetic Aperture Radar (InSAR) for the monitoring and risk assessment of geohazards near pipeline corridors. InSAR is a remote sensing technique that allows simultaneous measurements of surface deformation at regular intervals with high accuracy (millimetres), fine spatial resolution (several metres), and broad spatial coverage (hundreds to thousands km<sup>2</sup>).

InSAR results can be enhanced by integrating them with geomechanical models. Models such as 3DEC (a three-dimensional distinct element code) can yield additional important insights into landslide failure

mechanisms, where InSAR-derived displacements, both in space and time, provide an excellent constraint.

The goal of this work is to apply advanced InSAR techniques and geological/geomechanical models to detect, quantify, and model geohazard displacements. Section 2 describes the test site and data used in the analysis. Section 3 reviews the InSAR method used to derive surface displacements and presents InSAR-derived deformation maps of the unstable Alaskan Fels slope. Section 4 describes the 3DEC geomechanical model used in the analysis and presents preliminary results. A summary and discussion of further improvements to the combined InSAR/geomechanical modelling approach are given in Section 5.

## 2 TEST SITE AND DATA

### 2.1 Fels Glacier

Fels Glacier (63.4°N, 145.6°W) is located in the east-central Alaska Range in a steep-sided valley east of the Delta River. The Trans-Alaska Pipeline and Richardson Highway pass along the east side of the Delta River valley about 4 km west of the toe of Fels Glacier. The steep slopes above Fels Glacier are experiencing active deep-seated gravitational slope deformation (DSGD) (Newman 2013). The deforming area that is the subject of

this study is located north of the lowermost part of Fels Glacier and has a total area of nearly 7 km<sup>2</sup>, with slopes averaging approximately 15-25° and relief up to 850 m. The deforming slopes are underlain by muscovite- and quartz-rich schists with a pronounced foliation that dips 25-30° to the south-southwest. Figure 1 shows a portion of the Fels slope that displays scarps and disturbed terrain consistent with DSGSD.



Figure 1, Photograph of western Fels slope, Alaska, July 2010 (photo by Stephen Newman).

Deformation rates range from less than a millimetre to several centimetres per month and are spatially and temporally variable within the slope. The area has the potential for generating catastrophic rockslides or rock avalanches that could block Fels valley and might trigger debris flows or outburst floods that could damage the pipeline and highway below.

## 2.2 SAR Data

High-resolution space-borne SAR data were acquired over Fels Glacier and surrounding slopes between 2010 and 2011 using the RADARSAT-2 sensor. Two spotlight (SpotLight A or SLA) image stacks are available: one in ascending (Asc) and one in descending (Des) pass directions, enabling decomposition of InSAR-derived displacements into horizontal and vertical components. Multiple pass directions also provide coverage of slopes that may be occluded by shadow or suffer other geometric distortions in the opposite pass direction. Figure 2 illustrates footprints of the subsets of the Fels stacks considered in this analysis overlaid on Google Earth optical imagery.

A summary of the characteristics of each stack is given in Table 1. During processing the data were multi-looked in the azimuth direction to produce images with ~2 m resolution in both ground-range and azimuth directions. Other than occasional conflicts with higher-priority users, SAR imagery was acquired at a 24-day temporal interval for each stack.

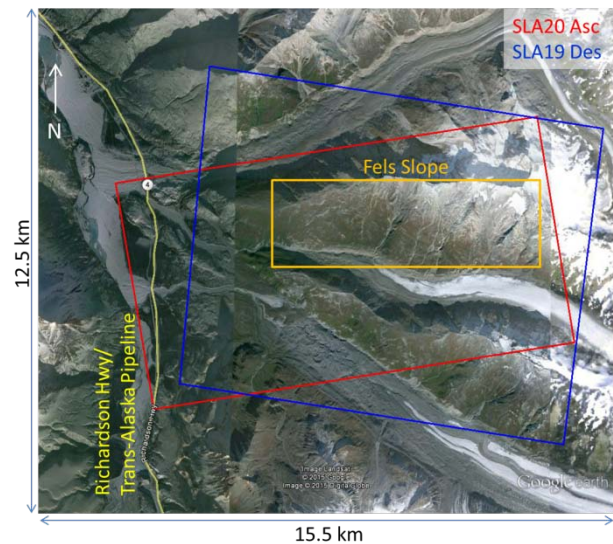


Figure 2, RADARSAT-2 data footprints of subsets of the SLA20 and SLA19 stacks overlaid on Google Earth optical imagery (Landsat, 2004-2007). The location of the deforming Fels slope and the Richardson Highway and Trans-Alaska Pipeline are also indicated.

Table 1. Summary of RADARSAT-2 Fels InSAR stacks.

Characteristic	SLA20	SLA19
Pass direction	Asc	Des
Incidence angle [°]	44.8	44.1
Satellite heading [°]	350.9	189.1
Ground-range resolution [m]	2.3	2.3
Azimuth resolution [m]	0.8	0.8
Swath (range x azimuth) [km]	19x9.2	19x9.6
Swath subset [km]	11.6x6.3	10.8x8.7
Number of scenes	24	24
Stack start date*	2010-01-04	2010-01-03
Stack end date*	2011-12-25	2011-12-24

\*YYYY-MM-DD

## 2.3 Ancillary Data

Ancillary data used in the analysis include Digital Elevation Models (DEMs) provided by the Alaska Department of Natural Resources (Hubbard et al. 2012) and the United States Geological Survey (U.S. Geological Survey 2013).

A high-resolution (1 m posting) LiDAR (Light Detection And Ranging) DEM from the Alaska Department of Natural Resources covered only a 3-5 km swath along the Trans-Alaska Pipeline. To complete coverage over the area of interest (AOI), a USGS 1/3 arcsecond (~10 m posting) DEM was merged with the LiDAR DEM and resampled to a posting of 4 m.

The Fels slope was studied by Stephen Newman as part of his MSc research at Simon Fraser University (Newman 2013). Newman documented the presence, spatial extent, and rates of DSGSD using field-geology methods and optical, SAR, and DInSAR (Differential InSAR) remotely-sensed images. He also documented

and mapped many of the morphological, geological, and structural characteristics of slopes undergoing DSGSD, and constructed simple numerical models to better understand potential deformation mechanisms.

### 3 SURFACE DISPLACEMENTS FROM INSAR

#### 3.1 InSAR Method

InSAR is an active remote sensing technology that measures the phase difference between waves returning to the sensor; this phase difference is related to the surface displacement between two acquisitions. Phase difference maps generated from all scene combinations in a stack are termed the network of interferograms. A more detailed overview of InSAR technology is available in Rosen et al. (2000).

With its high spatial and temporal resolutions, InSAR is potentially well suited for monitoring geohazards near pipeline corridors. However, InSAR is limited by temporal decorrelation due to changes in the scattering surface between acquisitions, including vegetation growth, rock falls, and snow cover. The InSAR phase also typically requires spatial filtering to reduce the phase noise present in a single pixel, while preserving deformation boundaries.

Our analysis uses a novel InSAR method, termed Homogenous Distributed Scatterer (HDS)-InSAR (Rabus et al. 2012). For each pixel, HDS-InSAR identifies nearby pixels with statistically similar amplitude distributions throughout the stack and averages the interferometric phase over this neighbourhood (Parizzi and Brčić 2011). This spatially adaptive averaging approach is able to suppress noise over distributed targets such as bare ground and asphalt while preserving high-quality point targets such as infrastructure and isolated rock outcrops. By averaging a pixel only with neighbours with similar scattering properties, the boundaries between areas representing different types of backscatter and presumably different deformation rates are preserved.

#### 3.2 InSAR Processing

Both SAR stacks over the Fels slope (Section 2.2) were processed individually using the HDS-InSAR processing chain shown in Figure 3. Areas with consistently low coherence such as the glacier surface and heavily vegetated regions were removed during the coherence-based point selection step.

The phase unwrapping step is particularly challenging for Fels due to its complex spatio-temporal deformation patterns and to decorrelation from persistent snow cover. The large phase gradients induced by rapid slope movements and the sharp phase discontinuities across scarps, tension cracks, and gullies make phase unwrapping of the network of interferograms difficult. For this reason, the analysis concentrated on the snow-free summer period of June to September and on interferograms with shorter temporal baselines (24 to 72-day interferograms) to avoid aliasing of the phase.

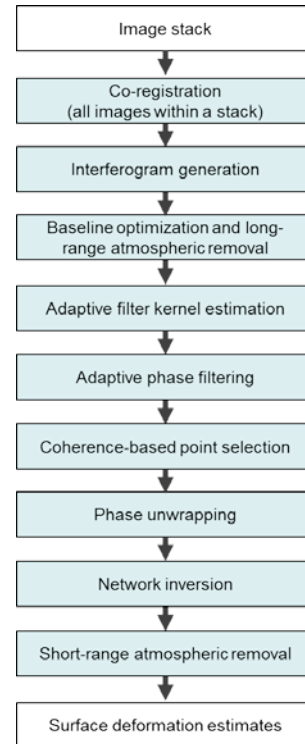


Figure 3, HDS-InSAR processing chain.

#### 3.3 Analysis of Line-of-Sight InSAR Displacements

The SLA19 and SLA20 stacks were processed independently to derive surface deformation estimates. As discussed in Section 3.2, seasonal snow cover between October and May over Fels rendered the interferometric phase of these periods unreliable. Some coherence was found between summer 2010 and 2011 scenes, but the phase was aliased over the Fels slope in these interferograms due to the large displacement magnitudes. Emphasis is thus on the cumulative deformation during individual summer seasons.

Figure 4 and Figure 5 show cumulative summer 2011 displacements measured in the radar line-of-sight (LOS) direction for the SLA20 (Asc) and SLA19 (Des) stacks, respectively. The approximate direction of the satellite look vector is indicated by the orange arrow. The white box denotes the area decomposed into east-west and vertical displacements components in Section 3.4.

Areas where the surface moves towards the radar are positive (shown in blue), areas moving away from the radar are negative (yellow/red), and green areas show negligible displacement in the LOS direction. The average radar intensity image over each image stack is shown in the background. All images are geocoded to North-up. Cumulative deformation maps were similar for summer 2010, but for brevity only the summer 2011 maps are displayed.

SLA20 (Asc, Figure 4) generally has higher point densities than SLA19 (Des, Figure 5), likely due to the relative orientation of the majority of slopes with respect to the radar look direction, where fewer slopes are in shadow in the ascending stack. SLA20 spatial coverage



also extends west of the Fels slope, where it is seen that the western area near the highway and Trans-Alaska Pipeline appears relatively stable. North of the Fels slope there appears to be anomalous net movement towards the radar in SLA20 (Figure 4); this may be due to residual atmospheric phase, which is difficult to characterize close to the image edge or to phase biases from late season snow on the north-facing slopes.

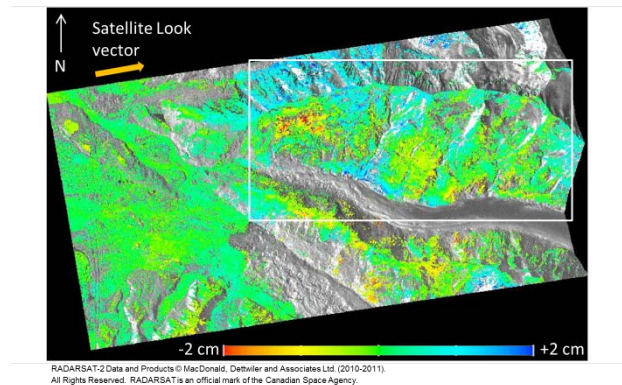


Figure 4, Line-of-sight cumulative deformation for SLA20 ascending stack for summer 2011 (2011-06-16 to 2011-09-20).

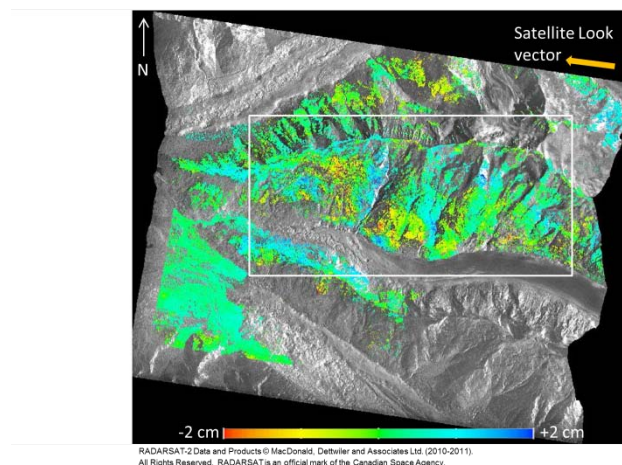


Figure 5, Line-of-sight cumulative deformation for SLA19 descending stack for summer 2011 (2011-06-15 to 2011-09-19).

The remainder of the AOI is active, with significant displacements of the Fels slope in both stacks. Surface deformation magnitudes vary considerably across the Fels slope. Results are consistent with Newman's (2013) field observation that the slope is divided into large-scale blocks ( $10^2$  to  $10^3$  m across) that may differentially deform relative to one another.

This complex deformation pattern results from the combined effects of spatially discontinuous and temporally sudden movement (e.g. landslides), progressive damage to the rock mass, and weather and climate variability (e.g. cyclic freeze-thaw).

### 3.4 InSAR Surface Displacement Decomposition

The SLA19 and SLA20 stacks acquired from opposing satellite pass directions were processed independently to derive a pair of LOS cumulative summer deformation estimates in Section 3.3. Because the time period over which cumulative summer displacement was measured was shifted only 12 hours between the descending and ascending stacks, no temporal interpolation of the surface displacements was necessary prior to their combination.

Each LOS measurement corresponds to the projection of the true three-dimensional deformation vector along the sensor LOS. With two LOS vectors and the near polar orbit of the satellite, only two of the three components can be retrieved: vertical and east-west displacements. Speckle tracking methods (e.g. Werner et al. 2001) can be used to derive displacement in the orthogonal (north-south) direction, although this technique is effective for only large displacements (significant fraction of a resolution cell) and coherent areas, and was not done for this study.

As the orthogonal component to the LOS is not exactly aligned with the north-south axis, the estimated vertical and east-west components are biased to a small degree (Eppler and Kubanski 2015). Using the SLA19 and SLA20 geometries from Table 1 and assuming equal displacement magnitudes in the north, east, and vertical directions, the bias in the inverted vertical and east-west components is, however, less than 15%.

The decomposition requires dense spatial sampling of coherent targets, therefore we carried out the decomposition only over the Fels slope (white box in Figure 4 and Figure 5), which has relatively high point densities in both ascending and descending passes. Decomposition was performed by interpolating the ascending and descending LOS displacements to a 5x5 m grid. Where multiple LOS measurements fell into a single grid pixel, the values were averaged together.

The two LOS vectors decomposed into vertical and east-west components are displayed in Figure 6 and Figure 7, respectively.

Decomposition into vertical and east-west components is important for the Fels site because LOS deformations cannot simply be projected downslope as complex spatially varying block displacements may exist. The DSGSD deformation at Fels can involve forward out-of-slope rotation and back-tilting of portions of the moving rock mass, in addition to downslope movement such as sliding and lateral spreading/creeping.

Figure 6 displays strong downward displacement on the northwest portion of the Fels slope, as well as in limited areas along the base of the Fels slope farther east; both of these displacements are considered consistent with downslope displacements when combined with the east-west motion from Figure 7. Significant uplift compatible with back-tilting is evident in the dark blue area along the base of the central Fels slope in Figure 6.

The two-dimensional decomposition of the InSAR results thus enables identification and mapping of surface displacement features, including their spatial extent, which might otherwise be difficult to determine from conventional surveys alone.

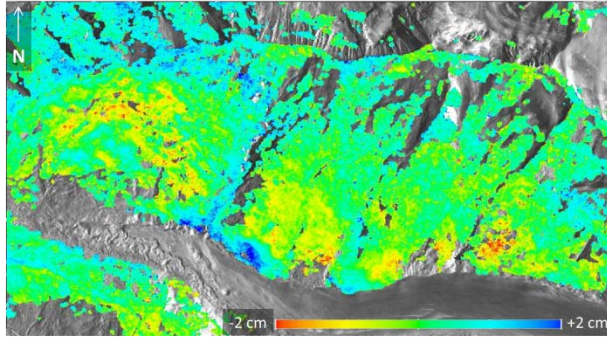


Figure 6. Vertical cumulative deformation (uplift positive, subsidence negative).

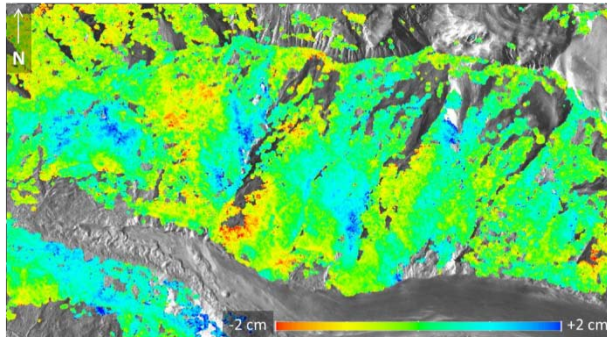


Figure 7. East-west cumulative deformation (east positive, west negative).

#### 4 GEOMECHANICAL MODELLING

Numerical models can yield additional important insights into landslide failure mechanisms. In this study, GIS interpretation and InSAR-derived displacements, both in space and time, constrain the geomechanical modelling.

We are developing the Fels geomechanical model in three main phases (Figure 8). The first phase was completed between 2012 and 2013 and comprised: 1) a field geological and engineering geological study, 2) InSAR analysis of a small area within the body of the landslide, and 3) a 2D distinct element analysis (DEM) of part of the landslide (Newman 2013). The main joint sets were identified during this phase (Table 2). The second phase, which is summarized in this paper, involves: 1) the GIS analysis and interpretation, 2) InSAR analysis of the entire landslide body, and 3) preliminary 3D distinct element modelling. The third phase, yet to be completed, involves additional engineering geological and terrestrial remote sensing surveys, more detailed GIS analyses, and an iterative InSAR/3D DEM study aimed at reproducing the behaviour and evolution of the landslide.

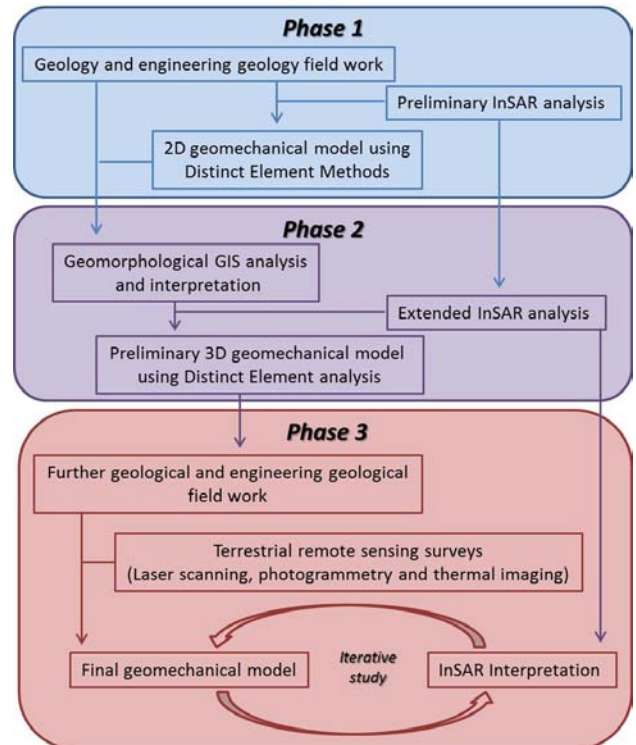


Figure 8. Flowchart showing the three phases of the geomechanical modelling study.

Table 2. Main discontinuity sets identified in the study area by Newman (2013).

Discontinuity set	Orientation	Dip
J1	SW-NE	Sub-vertical
J2	SE-NW	Sub-vertical
J3	E-W	Sub-vertical
S1	NNE-SSW	15°-25°

##### 4.1 Geomorphological Analysis and Interpretation Using GIS

We completed a detailed GIS analysis with the objectives of further understanding the landslide morphology and mechanism, and the influence of the geological structure and rock mass quality. The DEM data (Section 2.3) were interpolated to create varied thematic maps including “slope” and “aspect” maps representing the slope gradient and the slope dip direction, respectively. These thematic maps, together with a hillshade map, were used to further characterize the slope and to interpret the potential main landslide features such as discontinuities, tension cracks, and scars located within the slope. We ranked these features based on their linearity and continuity. We consider some of the features to be ‘uncertain’, requiring additional field work for verification during Phase 3 of the project.

Our preliminary GIS analysis indicates the presence of two main joint sets with SW-NE and SE-NW orientations, in agreement with Newman (2013) (Table 2). Figure 9 shows the slope map with recognized and inferred discontinuities.



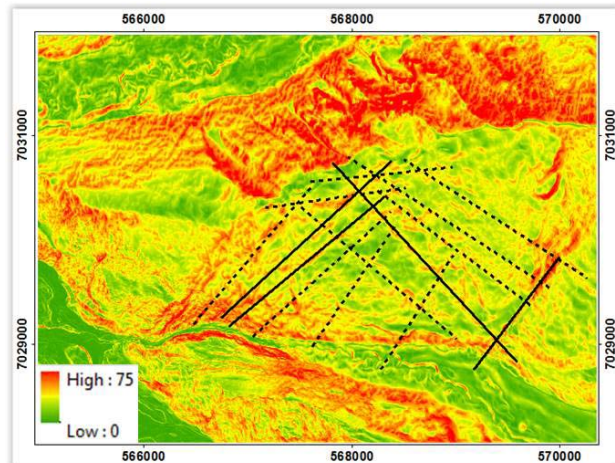


Figure 9, Slope map with the discontinuities. Solid lines are certain lineaments; dashed lines are uncertain lineaments requiring field confirmation.

#### 4.2 3D Distinct Element Analyses

We have previously shown that it is possible to use GIS to structurally characterize rock slopes. Francioni et al. (2014) and Wolter et al. (2013) showed that this information, together with the 3D geometry of the slope derived from a DEM, can be used to develop a 3D distinct element model of a landslide in 3DEC (Itasca 2014). The 3DEC code uses an explicit time-stepping scheme to solve Newton's equation of motion and treats the rock mass as a discontinuum material. In this context the discontinuities are the main control on rock mass behaviour as they cut the rock mass into blocks that can be assigned rigid or deformable stress-strain constitutive criteria depending on the rock mass characteristics (Cundall 1988). The Rhinoceros™ SR4 code (McNeel and Associates 2011) was used to create both the 3D model and the triangulated mesh starting from the DEM. The Kubrix software (Itasca 2014) was used to ensure the mesh is compatible with the 3DEC software.

In these preliminary 3DEC models we assume that the rock mass material consists of rigid blocks (non-deformable; density = 2600 Kg/m<sup>3</sup>). This assumption allows us to investigate the kinematic control of the discontinuity sets, and it also significantly reduces the required computer runtimes. Our focus in these preliminary geomechanical models is to understand the relationships between the slope failure kinematics, the observed geomorphic landform features, and the InSAR displacements.

Future 3DEC model simulations in Phase 3 of the study will incorporate a rock mass constitutive criterion (elasto-plasticity) in addition to discontinuity deformation. Incorporation of this criterion allows a more realistic representation of the landslide behaviour and improvement in the agreement between simulated and observed displacements. The joint properties used in these preliminary 3DEC models are shown in Table 3. Residual shear strength properties have been assumed at this stage to encompass the combined effects of tectonic and gravitational damage in addition to groundwater pressures.

Table 3, Joint properties used for the DEM simulation.

Properties	Value
Joint normal stiffness (Pa/m)	5E+9
Joint shear stiffness (Pa/m)	5E+8
Friction angle (°)	10
Cohesion (kPa)	0

Initially, two 3DEC geomechanical models were built using different discontinuum approaches:

- Model 1 - Model developed using the main, high-certainty geological structures recognized in the GIS analysis (solid lines in Figure 9) and the foliation discontinuity set previously mapped by Newman (2013);
- Model 2 - Model developed using all identified geological features recognized in the GIS analysis (including dashed lines in Figure 9 with their higher uncertainty) and the foliation planes (S1) previously mapped by Newman (2013) (Table 2).

The results of the simulations are draped on the hillshade map and presented in terms of displacements in the Z direction (vertical) in Figures 10B and C. Although both models show movements similar to those indicated by the InSAR analysis (Figure 10A), the second model more closely replicates the InSAR vertical motions. 2D N-S cross-sections through both of the 3DEC displacement models (see Figure 11 for Model 2) indicate that the simulated slope movements are relatively shallow, as noted in the previous UDEC results of Newman (2013). This result is in conflict with a DSGD failure mechanism and requires further research.

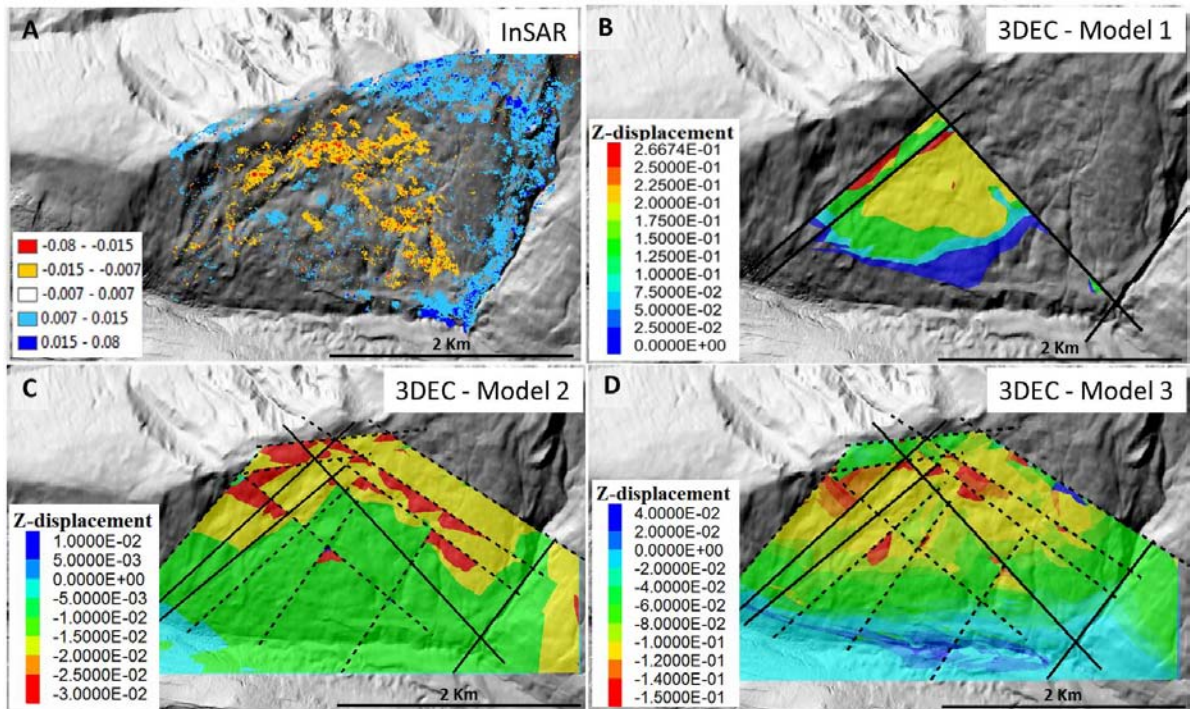


Figure 10, Vertical movement from the A) InSAR analysis and results of 3DEC simulations B) Model 1, C) Model 2, D) Model 3. Vertical cumulative deformation values from -0.005 m to 0.0005 m are excluded for clarity.

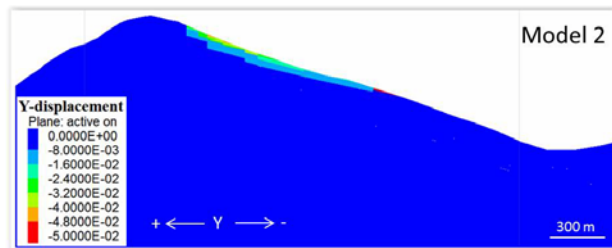


Figure 11, 2D N-S section through the 3DEC model showing Y displacements obtained using Model 2 and the indicated shallow nature of slope failure

In order to explore the controls on a shallow versus deep-seated slope displacement at Fels, a further 3DEC model was constructed:

- Model 3 - Model developed using all geological features recognized in the GIS analysis (solid and dashed lines in Figure 9), the foliation planes (S1), and an additional joint set dipping perpendicular to S1 with an E-W orientation (similar to J2 in Table 2) located at the toe of the slope.

Figures 10D and 12 show the results of this third series of model simulations in terms of displacements in, respectively, the Z and Y directions. Incorporation of the additional joint set leads to a new deeper sliding surface. This deep-seated failure may reflect a complex zone of movement involving interconnection between the foliation S1 and the orthogonal discontinuity set at the toe of the slope (Figure 13). A localized toe failure mechanism, in practice, may involve components of gravitationally

induced step-path failure in addition to failure of intact rock bridges. Moreover, as shown in Figure 10D, the use of Model 3 also results in areas at the slope toe exhibiting positive Z displacements (dark blue areas), which is in agreement with the InSAR data (Figure 6 and Figure 10A) and deep-seated slope deformation.

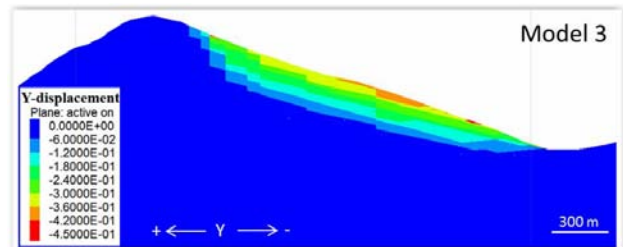


Figure 12, 2D N-S section through the 3DEC model showing Y displacements obtained using Model 3.

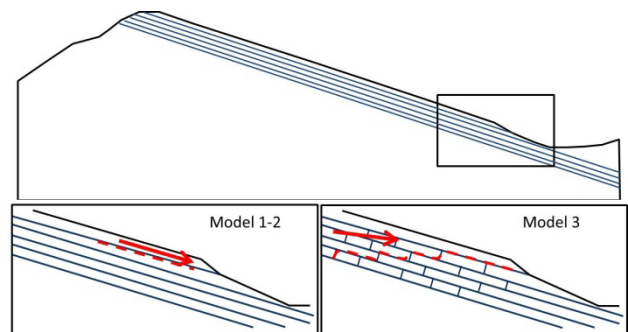


Figure 13, Conceptual representation of two possible slope toe-failure mechanisms generated in the 3DEC geomechanical models.

## 5 DISCUSSION AND CONCLUSIONS

InSAR surface displacements coupled with GIS analyses, field data, and geomechanical modelling can be used to improve our understanding of landslide geohazards along pipeline corridors and is a significant improvement over current monitoring practice.

GIS is a useful tool for locating tension cracks, lateral release scarps, and other geomorphic features, thereby providing information on historical spatial slope movements that are valuable input to geomechanical modelling.

InSAR documents the current deformation of the slope spatially and temporally. The use of multiple pass directions enables decomposition into horizontal and vertical displacement components. Despite the challenging conditions at Fels due to fast slope movements, sharp spatial discontinuities across cracks and gullies, and decorrelation from persistent snow cover, we were successful in quantifying deformation of the Fels slope in the summer months from InSAR. Incorporating InSAR data from subsequent summer seasons (2014 and 2015) would lend additional confidence to the validity of our results and enable an assessment of inter-annual displacement variability.

Field data including rock types, rock structure, and geomechanical properties are also important model inputs in attempting to reproduce the observed movements. Combined, these complementary forms of data can help calibrate geomechanical models. We have adopted three models for the preliminary 3DEC modelling of the Fels slope. Using Models 1 and 2 we showed the possibility of superficial landslide displacement controlled by two main joint systems (SE-NW and SW-NE) and a foliation plane directed NNE-SSW. Of these two approaches, Model 2 yields a better agreement with InSAR recorded displacements than Model 1.

With Model 3 we simulated the effects of an additional joint set orthogonal to the foliation, striking E-W and located at the slope toe. The introduction of this discontinuity set changed the simulated landslide from a shallow failure to a more deep-seated one (Figure 12). We will carry out additional geomechanical analyses (Phase 3) constrained by additional InSAR data and field observations with the objective of improving our understanding of the slope failure mechanism.

## ACKNOWLEDGEMENTS

This work is partially funded by the Canadian Space Agency (CSA) under the Earth Observation Application Development Program (EOADP) contract #9F043-130644/001/MTB. CSA also provided the RADARSAT-2 images. The authors acknowledge and thank Stephen Newman for his field work and initial modelling results at Fels as part of his Master's research.

## REFERENCES

- Cundall, P.A. 1988. Formulation of a three-dimensional distinct element model—part I. A scheme to detect and represent contacts in a system composed of many polyhedral blocks. *International Journal Rock Mechanics and Mining Sciences & Geomechanics Abstracts* 25 (3):107-116.
- Eppler, J. and Kubanski, M. 2015. Subsidence monitoring of the Seattle viaduct tunneling project with HDS-InSAR. In Proc. of the *Symposium on Field Measurement in Geomechanics (FMGM)*, Sydney, Australia, submitted.
- Francioni M., Salvini R., Stead, D. and Litrico S. 2014. A case study integrating remote sensing and distinct element analysis to quarry slope stability assessment in the Monte Altissimo area, Italy. *Engineering Geology*. 183, 290-302
- Hubbard, T.D., Koehler, R.D., and Combellick, R. A. 2012. *High-resolution lidar data for Alaska infrastructure corridors*. Technical Report File 2011-3, Alaska Division of Geological and Geophysical Surveys Raw Data File.
- Itasca. 2014. *3DEC version 5, Kubrix version 5*. Itasca Consulting Group Inc. Minneapolis, Minnesota. <http://www.itscag.com/3dec/>.
- McNeel and Associates, 2011. *Rhinoceros 4, SR9*. <http://www.rhino3d.com/download/rhino/4.0>.
- Newman, S.D. 2013. *Deep-seated gravitational slope deformations near the Trans-Alaska Pipeline, east-central Alaska Range*. MSc thesis, Simon Fraser University, Burnaby, BC.
- Parizzi, A. and Brcic, R. 2011. Adaptive InSAR stack multilooking exploiting amplitude statistics: A comparison between different techniques and practical results. *IEEE Geoscience and Remote Sensing Letters*, 8(3), 441-445
- Rabus, B., Eppler, J., Sharma, J., and Busler, J. 2012. Tunnel monitoring with an advanced InSAR technique. *Proceedings of SPIE (International Society for Optics and Photonics)*, 8361, 83611F–83611F–10.
- Rosen, P. A., Hensley, S., Joughin, I. R., Li, F. K., Madsen, S. N., Rodriguez, E., and Goldstein, R. M. 2000. Synthetic aperture radar interferometry. *Proceedings of the International IEEE*, 88(3):333-382.
- U.S. Geological Survey. 2013. *USGS NED n64w147 and n64w146 1/3 arc-second 2013 1 x 1 degree ArcGrid*. U.S. Geological Survey.
- Werner, C., Strozzi, T., Wiesmann, A., Wegmüller, U., Murray, T., Pritchard, H., and Luckman, A. 2001. Complimentary measurement of geophysical deformation using repeat-pass SAR. In Proc. of the *IEEE International Geoscience and Remote Sensing Symposium (IGARSS)*, 7, 3255-3258.
- Wolter, A., Zorzi, L., Stead, D., Clague, J.J., Genevois, R. and Ghirotti, M. 2013. Exploration of the kinematics of the 1963 Vajont slide, Italy, using a numerical modelling toolbox. *Italian Journal of Engineering Geology and Environment*. Book Series 6, pp. 599 - 612